ACS APPLIED MATERIALS & INTERFACES

Research Article

www.acsami.org

Enhanced Photoreduction CO_2 Activity over Direct Z-Scheme α-Fe_2O_3/Cu_2O Heterostructures under Visible Light Irradiation

Ji-Chao Wang,[†] Lin Zhang,[†] Wen-Xue Fang,[†] Juan Ren,[†] Yong-Yu Li,[‡] Hong-Chang Yao,*[,†] Jian-She Wang,[†] and Zhong-Jun Li*[,†]

[†]College of Chemistry and Molecular Engineering, Zhengzhou University, Zhengzhou 450052, China

[‡]Department of Chemistry, Zhengzhou Normal University, Zhengzhou 450044, China

Supporting Information

ABSTRACT: Hematite−cuprous oxide (α-Fe_2O_3/Cu_2O) nanocomposites are synthesized based on the design of Z-scheme photocatalyst for CO_2 reduction. The band structure for the typical Fe_2O_3/Cu_2O (with 1:1 mole ratio) is characterized by UV−vis reflectance spectroscopy and X-ray/ultraviolet photoelectron spectroscopy, and its heterojunction is determined to be Type II band alignment. The photoreduction CO_2 activities of the heterostructures are investigated in the presence of water vapor. The CO yields are changed with Fe/Cu mole ratio, and the maximal CO yield attains 5.0 μmol·g cat^{-1} after 3 h of visible-light irradiation. Besides the effect of light wavelength, H_2O/CO_2 molar ratio and temperature on the products is studied. The selectivity of the prepared catalysts is tunable by modulating the light wavelength. The reaction mechanism is proposed and further confirmed experimentally. The results gained herein may provide some insights into the design of Z-scheme photocatalysts for CO_2 reduction.

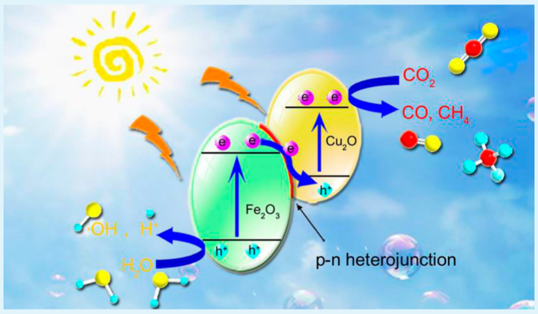

KEYWORDS: *CO_2 reduction, Fe_2O_3/Cu_2O composite photocatalyst, visible-light-activated photocatalysis, Z-scheme*

1. INTRODUCTION

The growing concerns about the emission of anthropological carbon dioxide (CO_2) and the depletion of fossil resources have driven research interests in developing technologies that can facilitate the capture, sequester and recycle of CO_2.[1−3] Among the different technologies, solar photocatalytic conversion of CO_2 to renewable fuels is regarded as a fascinating way that not only addresses global warming but also partly fulfills energy demands.[3−5] Photocatalysts play a vital role in the conversion process and hence, developing efficient visible-light-driven (VLD) photocatalysts has been an active field of intensive research.

Since Inoue et al.[6] first reported photoreduction of CO_2 to organic compounds in 1979, much effort has been focused on extending the light response of TiO_2 to the visible region.[7,8] However, only limited success was achieved due to the wide band gap of the matrix TiO_2 (3.0−3.2 eV). Recently, several native VLD semiconductors for CO_2 reduction have been developed, but the efficiencies are still far from practical applications due to fast charge recombination.[9−11] To overcome the serious drawbacks of the limited visible-light absorption and fast charge recombination of semiconductor photocatalysts, researchers, over the past few decades, have explored different strategies such as band-structure engineering, heterostructured constructing, and nanostructuralization, and the most widely used one is to develop photocatalytic heterojunctions.[12,13]

Among the numerous heterojunction photocatalysts, the p−n heterostructured systems with a staggered (Type II) band alignment have been drawing much attention due to their efficient charge separation.[14] There are mainly two charge transfer modes across the p−n junctions for Type II heterostructures. One mode is double-charge transfer, in which the photoinduced electrons transfer to one semiconductor with a more positive conduction band (CB) while holes transfer to one with a more negative valence band (VB). This mode is unfavorable for CO_2 reduction because it leads to a low reduction potential. By contrast, another mode, Z-scheme type, in which the charge transfer directly quenches the weaker oxidative holes and reductive electrons, is preferable.[15] More importantly, the product selectivity of CO_2 reduction may be tuned by modulating the band alignment via selecting the components and proportion.[3] Previous studies adopted Z-scheme systems for various photocatalytic reactions, including hydrogen production, water splitting and pollutant degradation.[16−18] However, Z-scheme systems for CO_2 reduction have been scarcely reported until now.[19,20] Besides, the visible-light responding components in these systems are restricted to metal complex that is easily oxidized, probably leading to efficiency reduction and material instability. It is thus highly desirable to

Received: January 28, 2015
Accepted: April 7, 2015
Published: April 7, 2015

DOI: 10.1021/acsami.5b00822
ACS Appl. Mater. Interfaces 2015, 7, 8631−8639

develop novel Type II band alignment heterostructures via Z-scheme transfer with high efficiency and stability.

First-row transition metal oxides are inexpensive potential alternative materials for solar energy conversion. For example, hematite (α-Fe_2O_3) is a VLD n-type semiconductor (2.2 eV) that can adsorb light up to 600 nm.[21] The narrow bandgap coupling with its valence band edge (2.48 eV) makes it an excellent catalyst for photochemically oxidizing water.[22] Nevertheless, the flat-band potential of electrons in the conduction band of Fe_2O_3 is lower than that required for CO_2 reduction. In contrast, cuprous oxide (Cu_2O) is an intrinsically p-type semiconductor with a bandgap of 2−2.2 eV and a conduction band site at −1.15 eV, making it an ideal photocatalyst[11] or co-catalyst[23−25] for CO_2 reduction. Unfortunately, hematite is known to have an extremely short hole diffusion length (<10 nm) and short excitation lifetimes (~10 ps),[26] while Cu_2O is known to have photostability problem.[27] An effective way to address these issues may be provided by coupling them to construct an adequate interface connection to realize Type II or direct Z-scheme electron transportation, as predicted by Mirtchev et al.[28]

Apart from the charge transfer mode, the intrinsic physicochemical properties of semiconductors, such as band gap, band edge positions, particle size and morphology, exact great influences on the photocatalytic performance of semiconductors.[29,30] Among them, the positions of electronic band edges are an important metric for determining a material's capability to function in a solar conversion system.[31] For the heterojunction semiconductors, it is of significance to accurately determine the conduction and valence band offsets, which dictate the degree of charge carrier separation and localization.[32] However, for the most heterojunctions, the interface band alignment parameters have been rarely reported so far.

In the present study, we select p-type Cu_2O and n-tpye α-Fe_2O_3 as components to design efficient VLD photocatalyst for CO_2 reduction. Type II α-Fe_2O_3/Cu_2O hetrostructures are constructed via a hydrothermal-deposition followed by Vitamin C reduction method. Detailed investigations on the photocatalytic CO_2 activity of Fe_2O_3/Cu_2O nanoparticles were carried out in the presence of water vapor. The influences of external conditions including irradiation intensity, H_2O/CO_2 molar ratio, and reaction temperature on the photocatalytic activity are also studied. Compared to pure Fe_2O_3 and Cu_2O, the as-prepared Fe_2O_3/Cu_2O nanocomposites are found to exhibit highly improved photocatalytic performance, and the selectivity of which is able to be tuned by modulating the light wavelength. The enhanced catalytic activity is attributed to the efficient charge separation originated from the Type II band structure, and a Z-scheme charge transfer mechanism is further proposed and confirmed.

2. EXPERIMENTAL SECTION

2.1. Catalyst Preparation. A series of Cu_2O/Fe_2O_3 composite catalysts were obtained through depositing the Cu_2O precursor onto the surface of α-Fe_2O_3 nanoparticles. In a typical experiment, a solution of ferric nitrate nonahydrate (2.02 g) in *n*-butanol (10 mL) was sealed in a Teflon-lined stainless steel autoclave and heated at 160 °C for 24 h. The product was mixed with a different concentration solution of cupric sulfate, and then, an appropriate amount of sodium hydroxide solution (1.0 mol/L) was added dropwise. Afterward, the deposit was reduced by Vitamin C according to the literature method.[33] Samples with different mole ratio of Fe/Cu were thus obtained after drying at 70 °C for 12 h. The resulting specimens are labeled as *x*CuFe, where *x* stands for the Cu_2O mol % in the samples. For comparison, we also prepared pure Fe_2O_3 and Cu_2O under the same conditions.

To verify the authentic ratio of Fe/Cu in the final composites, the content of metal cations was measured by inductively coupled plasma atomic emission spectroscopy (ICP-AES), and the analytical results are given in Table S1 (Supporting Information). As can be seen, the obtained Fe/Cu atomic ratios are larger than the nominal values, suggesting that a small amount of Cu was lost in the precipitation process.

2.2. Catalyst Characterization. Powder X-ray diffraction intensities were recorded with X-ray diffractometer (PANalytical X'pert PRO, Netherlands). The composition for the *x*Cu−Fe composites was determined by ICP-AES analysis using Thermo Scientific iCAP 6000 spectrometry. Nitrogen adsorption−desorption isotherms were collected on a NOVA 1000e surface area and porosity analyzer (Quantachrome, Boynton Beach, FL). Transmission electron microscopy (TEM) was performed on a Tecnai G^2 20 S-TWIN electron microscope. As further evidence, high-resolution transmission electron microscopy (HRTEM) was employed and the corresponding fast Fourier transform (FFT) was obtained by Gatan Digital Micrograph software (Gatan, Inc., Pleasanton, CA).

X-ray photoelectron spectroscopy (XPS) measurements were carried out at room temperature on a PerkinElmer PHI 5300 X-ray Photoelectron Spectrometer. Al Kα radiation ($h\nu$ = 1486.6 eV) was adopted as the excitation source and the binding energies were corrected using the background C 1s peak (284.6 eV) as a reference. The peak position was estimated using a fitting procedure based on summation of Lorentzian and Gaussian functions using the XPSPEAK 4.1 program.[34] Ultraviolet photoelectron spectroscopy (UPS) data was obtained with HeI (21.2 eV) as monochromatic light source. UV−vis diffuse reflectance spectra (DRS) were obtained using an UV−vis spectrometer (Cary 5000). Photoluminescence (PL) spectra were measured with a LifeSpec-II fluorescence spectrometer equipped with an EPL488 laser diode. Photoelectrochemical test was recorded by a CHI 660 E electrochemical workstation (Chenhua, Shanghai, China).

2.3. Photocatalytic Performance Tests. Prior to CO_2 photoreduction experiments, the reaction setup was vacuum-treated and scavenged with a mixture of the high purity CO_2 gas (99.995%) and water vapor for five times. Then, compressed CO_2 gas was passed through a water bubbler to generate a mixture of CO_2 and H_2O vapor. The reactant CO_2/H_2O gas was introduced to a stainless steel cylindrical reactor, at the bottom of which, 10 mL of deionized water was pre-added to tune the saturated water vapor pressure through controlling the reaction temperature. After being dispersed uniformly with a fixed amount of 0.10 g catalyst powder, a circular glass dish was fixed at the center of the reactor, equipped with a quartz window for passing light irradiation from the reflector lamp located above the vessel. The light source used to activate the photocatalytic reactions was a 300 W xenon arc lamp (PLS-SXE300, Beijing Trust Tech Co., Ltd., China) with a UV cutoff filter (λ > 400 nm). The light intensity was modulated to 164 and 260 mW cm^{-2}, respectively, to study the impact of light intensity on the products. The reactor temperature was controlled by a constant temperature apparatus. After irradiating for a given period of time, 3.00 mL of the gaseous products was taken from the reactor using a gas chromatograph (GC-7890 II, Techcomp Corp., China) equipped with a flame ionized detector (FID) and a thermal conductivity detector (TCD) for the analysis of methane, carbon monoxide, carbon dioxide, and oxygen. The FID detector was connected with a TDX-01 column, and the TCD detector with a porapak-Q column. The quantification of the yield of CH_4, CO and O_2 was based on the external standard and the use of a calibration curve.

Blank tests were first conducted in the absence of photocatalysts or in the dark with catalysts. No product was detected, indicating that the presence of both the visible-light irradiation and photocatalyst are indispensable for the photocatalytic reduction of CO_2 with water. To assess the stability of the synthesized composites, a sample 50Cu−Fe as a model was refreshed by immersing it in Vitamin C alkaline solution and reevaluated its photocatalytic performance.

DOI: 10.1021/acsami.5b00822
ACS Appl. Mater. Interfaces 2015, 7, 8631−8639

2.4. Analysis of Hydroxyl Radicals (•OH). The formation of hydroxyl radicals (•OH) on the surface of *x*Cu/Fe composites was detected by the PL technique using terephthalic acid (TA) as a probe molecule. It has been proven that TA reacts readily with •OH to produce 2-hydroxyterephthalic acid (TAOH) with a characteristic fluorescent signal at 425 nm,[35] and the intensity of the peak attributed to TAOH is proportional to the amount of hydroxyl radicals formed.[36] The detection procedures were similar to the photoreduction experiments, except that the catalysts were replaced by the mixture of the catalyst and TA (1:1 weight ratio). Sampling was carried out at given irradiation time intervals, and then, the obtained samples were dispersed in deionized water. The suspension was filtered after centrifugation, and the resulting solution was set to the same concentration for fluorescence spectral measurements. The maximum PL intensity of TAOH was detected at 425 nm with excitation at 315 nm using a fluorescence spectrophotometer (Hitachi F-7000).

3. RESULTS AND DISCUSSION

3.1. Structure and Morphology. Figure 1 shows the representative XRD patterns of *x*Cu−Fe composites with x = 30, 50, and 70 mol % along with pure Fe_2O_3 and Cu_2O for comparison. It can be seen that the diffraction peaks of pure Fe_2O_3 match perfectly with those of alpha phase of hematite (PDF No. 01-086-2368), whereas the diffraction patterns of pure Cu_2O are in good agreement with those of cubic phase of Cu_2O (PDF No. 01-078-2076). For the *x*Cu−Fe composites, all the XRD patterns can be well indexed to the hematite phase of Fe_2O_3 and cubic phase of Cu_2O with no appearance of a third phase. In addition, the cubic Cu_2O diffraction peaks begin to appear and gradually intensify, while the peaks of α-Fe_2O_3 weaken regularly with increasing of Cu_2O contents. This can be obviously seen from the variation of the typical (111) crystal plane of Cu_2O and (104) and (110) crystal planes of Fe_2O_3.

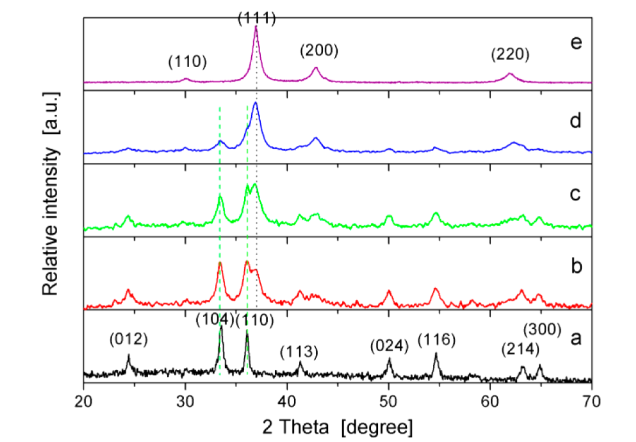

Figure 1. XRD of Fe_2O_3(a), Cu_2O(e), and *x*Cu−Fe (x = 30, 50, and 70% labeled as b, c, and d, respectively).

Representative TEM patterns of the 50Cu−Fe photocatalyst are displayed in Figure 2. As shown in Figure 2a, the obtained 50Cu−Fe sample consists of nanoparticles with partial agglomeration. The size distribution histogram, measured 150 nanoparticles using Gatan software, is shown to center at 11 ± 5 nm (Figure S1, Supporting Information). Moreover, the agglomerate of nanoparticles results in the formation of mesopores between the particles, which is demonstrated by BET measurements and pore-size calculations (see Supporting Information, Figures S2 and S3). A high-resolution TEM image of 50Cu−Fe with representative heterostructures is shown in Figure 2b. Fast-Fourier transform (FFT) diffraction patterns of

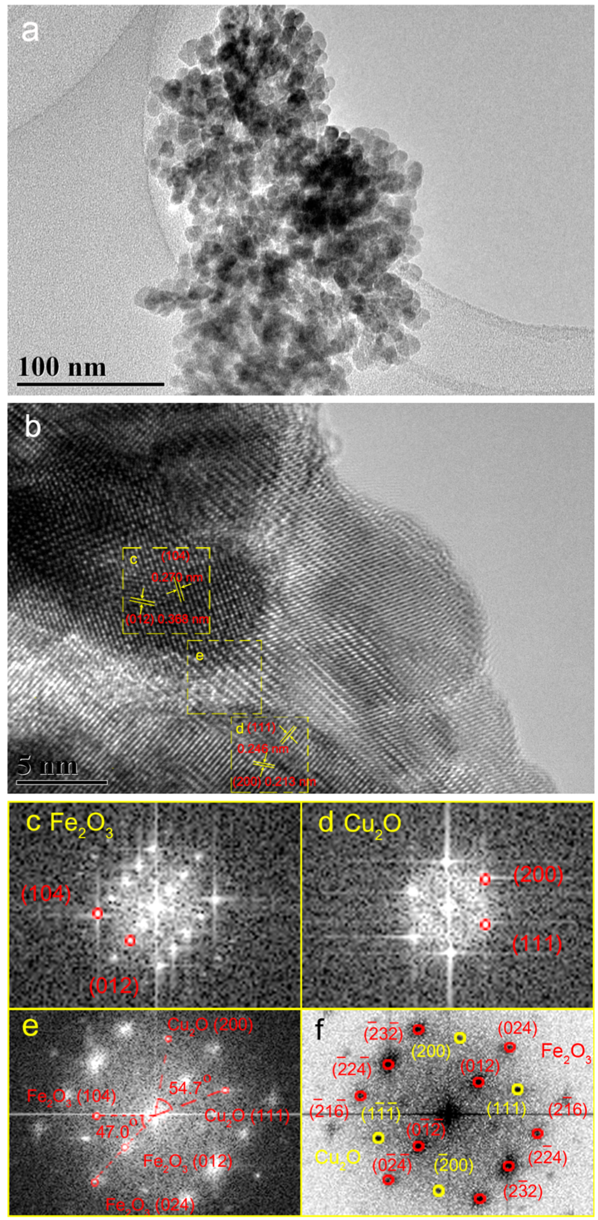

Figure 2. (a) TEM image of 50Cu−Fe nanoparticles; (inset) distribution of isolated single particles. (b) High-resolution TEM image of selective area in the 50Cu−Fe composite. (c−e) Simulated FFT patterns and the indexed diffraction spots separated from the area of square outlines in panel b. (f) Experimental FFT patterns with diffraction spots indexed to the planes of α-Fe_2O_3 and Cu_2O.

selected areas for α-Fe_2O_3 and Cu_2O regions as well as heterojunction region along with their simulated FFTs are shown in Figure 2c−e. From the clearly resolved d spacing of 0.270 and 0.368 nm in region c, (104) and (012) facets can be assigned to the observed lattice fringes for α-Fe_2O_3, and its corresponding simulated FFT pattern allows us locating the highlighted spots to be well indexed to the two planes (Figure 2c). The zone axis was calculated from the cross product of the two vectors perpendicular to the (104) and (012) planes. The junction plane for α-Fe_2O_3 is thus assigned to be (012) with the $[42\bar{1}]$ zone axis. Similar analysis in region d resulted in the (111) junction plane of cubic Cu_2O along with the $[01\bar{1}]$ axis direction (Figure 2d). The observed junction plane pairs, such as $(012)_{\alpha\text{-}Fe_2O_3}/(111)_{Cu_2O}$ with the $[42\bar{1}]$ and $[01\bar{1}]$ zone axes,

DOI: 10.1021/acsami.5b00822
ACS Appl. Mater. Interfaces 2015, 7, 8631−8639

suggest the formation of heterostructural nanocrystals.[37] The diffraction spots in the FFT pattern for region e can be well indexed to the planes of α-Fe_2O_3 and Cu_2O (Figure 2e), which is well in agreement with that of the experimental diffraction patterns shown in Figure 2f. The high-resolution TEM observations and the assigned FFT patterns of 50Cu−Fe heterostructures, consistent with XRD results, reveal both Cu_2O and α-Fe_2O_3 phase to be present and fused at the interfaces.

3.2. Surface Chemical Composition and Electronic State. The surface chemical compositions and the valence states of Fe and Cu ions of 50Cu−Fe composites were identified by XPS. A survey scanning spectrum of typical 50Cu−Fe sample indicates that main constituent elements of the composite are Fe, Cu, and O atoms, except for an additional peak resulting from C element (Figure S4, Supporting Information). In the high-resolution Fe 2p spectrum (Figure 3a), two distinct peaks at binding energies of 711.0 eV for Fe $2p_{3/2}$ and 724.4 eV for $2p_{1/2}$ are observed, consistent with those reported in Cu_2O/Fe_2O_3 nanotubes.[38] In addition, two satellite peaks at 717.4 and 732.6 eV is clearly distinguishable, agreeing well with those of published results.[39]

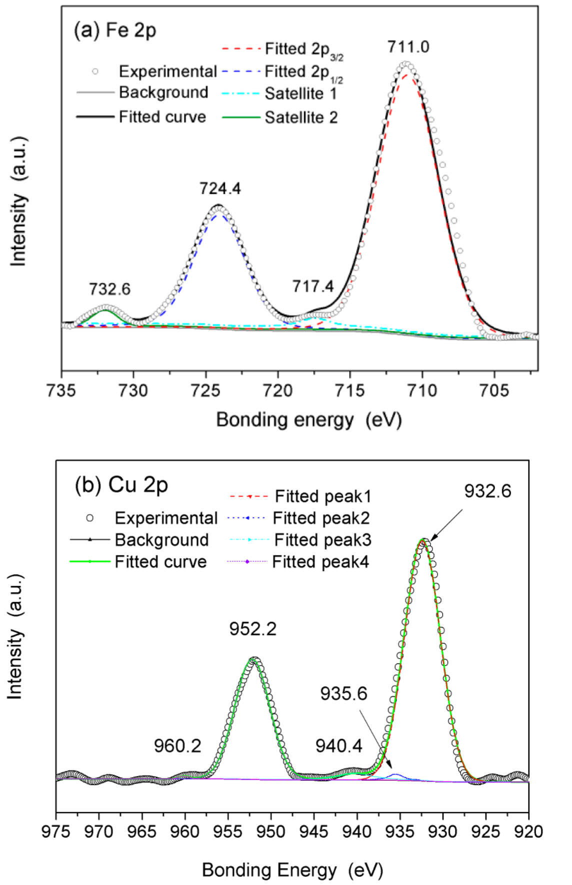

Figure 3. XPS high-resolution spectra and the corresponding Gaussian−Lorentzian fits of (a) Fe 2p and (b) Cu 2p of the 50Cu−Fe composite.

The Cu 2p core level spectrum and the deconvolution results are shown in Figure 3b. Two broad peaks centered at ∼933 and ∼952 eV are found, corresponding to the binding energies of the Cu $2p_{3/2}$ and $2p_{1/2}$ levels, respectively. The deconvolution of Cu $2p_{3/2}$ peak reveals a main peak at 932.6 eV and accompanied by two satellite peaks on the high-binding-energy side, 935.6 and 940.4 eV, respectively. The fitted peaks at 932.6 and 952.2 eV are characteristic of Cu^+ $2p_{3/2}$ and $2p_{1/2}$,[38] while the fitted shakeup peaks at 935.6 and 940.4 eV, as well as the satellite peak at 960.2 eV, are characteristic of CuO having a d^9 configuration in the ground state.[40] The presence of Cu^{2+} ions may be originated from ambient oxidation of Cu^+ on the sample surface. This phenomenon had been reported by many researchers on the synthesis of Cu_2O nanoparticles.[40,41] It is noteworthy that the observed peaks related with the Cu^+ $2p_{3/2}$ and $2p_{1/2}$ (at 932.6 and 952.2 eV) are much stronger than the peaks related with Cu^{2+} $2p_{3/2}$ and $2p_{1/2}$, implying that the chemical valence of Cu is mainly +1.

The deconvolution peaks of the O 1s spectrum could be resolved into five components, including lattice oxygen, lattice hydroxyl, and adsorbed water (Figure S5, Supporting Information). The existence of hydroxyl at the surface of the composites is important because the H_2O molecules can be easily accessible to the surface of materials, leading to higher activity for CO_2 photoreduction.[42]

3.3. UV−Vis Diffuse Reflectance Spectra. To investigate the light-harvesting ability of the catalysts, we examined UV−vis diffuse reflectance spectra (DRS) of pure α-Fe_2O_3, Cu_2O, and xCu−Fe composites (x = 20−80) in the range of 350−750 nm; the results are shown in Figure 4. A regular red-shift with the increment of Cu content is observed for the composites. More importantly, the composites show strong absorption in the visible light region, indicating the feasibility of utilization of visible light for CO_2 photoreduction. The band gaps (E_g) of the samples were estimated by the plot of $(\alpha h\nu)^2$ versus photo energy ($h\nu$), considering that Fe_2O_3[43] and Cu_2O[44] exhibit band-to-band excitations involving indirect transitions (Figure S6, Supporting Information). The calculated E_g value of α-Fe_2O_3 is 1.97 eV, agreeing well with the reported values of α-Fe_2O_3,[45] while the E_g of Cu_2O is 2.05 eV, consistent with the previously reported values of Cu_2O (2.0−2.2 eV[41]). The E_g values of the composites are found to fall between those of the pure materials (Table S2, Supporting Information). However, due to the approximate band gap values, the contrasts are subtle but still related with the content of Cu_2O.

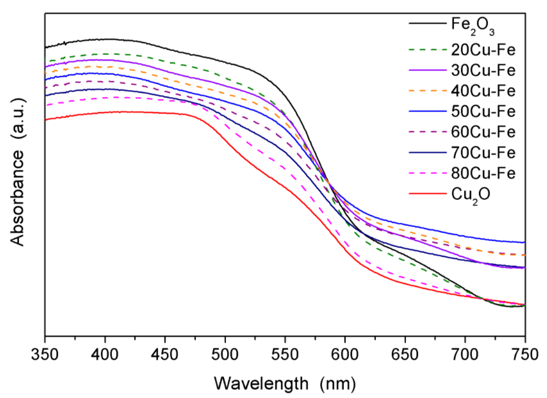

Figure 4. UV−vis diffuse reflectance spectra of different samples.

3.4. Band Alignment. The band edge positions of the prepared composites are of critical importance because of their direct influence on the redox reactions occurring at the particle surface. The combination of UV−vis absorption spectra with ultraviolet photoelectron spectra and XPS valence band spectra was used to determine electronic band alignments. Figure 5

DOI: 10.1021/acsami.5b00822
ACS Appl. Mater. Interfaces 2015, 7, 8631−8639

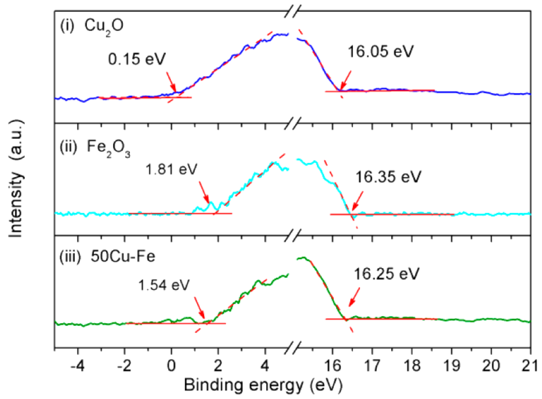

Figure 5. Ultraviolet photoelectron spectra of (i) Cu_2O, (ii) Fe_2O_3, and (iii) 50Cu−Fe.

shows the UPS spectra of Cu_2O, Fe_2O_3 and 50Cu−Fe measured at sample biases (−8 V). According to the linear intersection method,[46] the valence band maximum (E_{VB}) of Cu_2O was estimated to be located at −5.32 eV (vs vacuum). The work function and the corresponding Fermi level (E_F) of Cu_2O was calculated to be 5.17 and −5.17 eV (vs vacuum), respectively. Because the E_g value of Cu_2O is 2.05 eV, the conduction band minimum (E_{CB}) is ca. −3.27 eV (vs vacuum). The corresponding relative VB and CB positions are 0.88 and −1.17 eV (vs. NHE), respectively, according to the relationship between the vacuum energy (E_{abs}) and the normal electrode potential (E^{θ}), $E_{abs} = -E^{\theta} - 4.44$.[46] Similarly, the values of E_{VB}, E_{CB}, and E_F of Fe_2O_3 can be determined by DSR and UPS.

When p-Cu_2O and n-Fe_2O_3 are in contact, alignment of the Fermi levels at the 50Cu−Fe material interface is assumed.[47] In this case the band offsets of the composite can be calculated using XPS core-level alignment method.[48] The XPS core-level spectra of the pure materials and the heterostructure 50Cu−Fe are shown in Figure S7 (Supporting Information). According to the conventional method,[49] the ΔE_{VB} and ΔE_{CB} for 50Cu−Fe are calculated to be 1.69 ± 0.05 and 1.77 ± 0.08 eV, respectively. In comparison with those before in contact, both ΔE_{VB} and ΔE_{CB} of the composite rise up about 0.3 eV. Provided that the difference value (D-value) between CB and E_F of Fe_2O_3 as well as D-value between VB and E_F of Cu_2O keeps constant before and after contacting, and that the possible band bending is neglected,[50] the valence band maximum of Fe_2O_3 in 50Cu−Fe is calculated to be 2.39 eV (vs. NHE), and the conduction band minimum of Cu_2O in 50Cu−Fe is calculated to be −1.32 eV (vs. NHE). The obtained values are summarized in Table S3 (Supporting Information). Correspondingly, a scheme of the band structure diagram isshown in Figure 6. It can be seen that a Type II (staggered) band alignment heterostructure is successfully constructed, and sufficient reductive potential for CO_2 reduction is attained.

3.5. Photocatalytic Performance for CO_2 Reduction with H_2O.

The photocatalytic CO_2 reduction experiments for the prepared xCu−Fe (x = 0−100) were carried out in the presence of water vapor under visible-light irradiation. To validate the role of the heterojunctions on the photocatalytic activities, the photoreduction CO_2 efficiency was measured for the composites with different Cu/Fe molar ratio. The results show that the predominant reaction product is CO under visible light with intensity of 164 mW cm^{-2}, no other products such as CH_4 are detectable. Figure 7 shows the dependence of

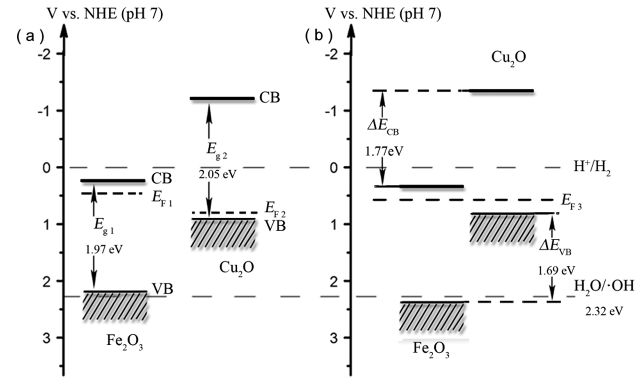

Figure 6. Diagram of the (a) band energy of Cu_2O and Fe_2O_3 before contact and (b) the energy band alignment of Cu_2O/Fe_2O_3 heterojunction. (E_{F1}, E_{F2}, and E_{F3} represent to the Fermi levels of pure Cu_2O, Fe_2O_3, and heterostructures, respectively.).

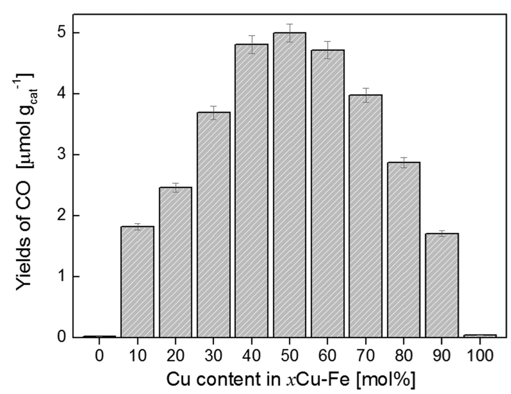

Figure 7. Yields of CO for xCu−Fe (x = 0−100) under visible light irradiation with 164 mW cm^{-2} intensity for 3 h at the H_2O/CO_2 ratio of 0.025 and the temperature of 40 °C.

CO yields on the Cu content; the yield of CO first increases and then decreases, dependent on the Cu_2O content. The sample 50Cu−Fe exhibits the highest photocatalytic activity with 5.0 μmol g_{cat}^{-1} yield. Moreover, the CO yields of all the composite samples display significantly higher than that of pure Fe_2O_3 and Cu_2O. The results suggest that the photoactivity for the investigated system is intensively related to the formation of the heterojunctions. To corroborate this heterojunction effect, we carried out further contrast tests. The results show that no products such as CO and CH_4 were detected for all the mechanically mixed Fe_2O_3−Cu_2O samples with similar particle sizes, indicating that the loosely contacted interfaces are insufficient for photocatalytic reduction of CO_2. The above results demonstrate the importance of the formed heterojunctions in enhancing photocatalytic activity.

Apart from the intrinsic properties, the photoactivity usually depends on the experimental conditions, such as the type of light, light intensity, CO_2/H_2O molar ratio, and temperature.[51] The effect of reaction temperature on the photocatalytic activity was examined on 50Cu−Fe catalyst. The results show that the photocatalytic activity was not significantly sensitive to temperatures between 5 and 60 °C (Figure S8, Supporting Information), which is in accordance with the results of Fox and Dulay.[52] The reaction temperature is hence set to 40 °C in the experiments.

Figure 8 shows CO yields of the 50Cu−Fe catalyst under the condition of the constant pressure of 0.3 MPa with different

DOI: 10.1021/acsami.5b00822
ACS Appl. Mater. Interfaces 2015, 7, 8631−8639

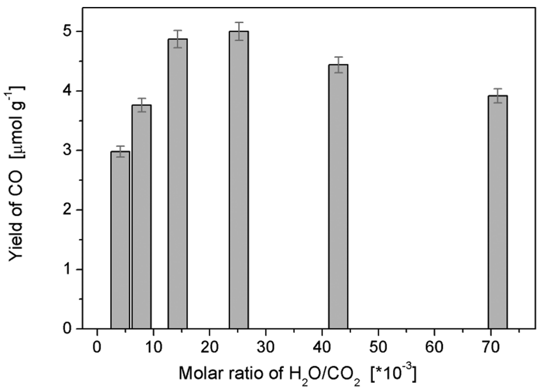

Figure 8. Influence of H_2O/CO_2 molar ratios on the CO yield of 50Cu−Fe catalyst under visible-light irradiation with 164 mW cm^{-2} intensity for 3 h at the temperature of 40 °C.

CO_2/H_2O molar ratio. The CO yield increases with CO_2/H_2O molar ratio, but decrease after reaching a maximum value 5.0 μmol g^{-1} at the H_2O/CO_2 ratio of 0.025. The results may be explained by the different adsorption capacity of CO_2 and H_2O molecules on the surface of the catalyst. The water molecule can be readily accessible to the surface of catalyst with hydroxyl because of its higher polarity than that of CO_2, as evidenced by Zhang and co-workers.[53] Appropriate H_2O molecules adsorbed are favorable for CO_2 reduction through reacting with holes. However, too much H_2O molecules absorbed may occupy more active sites on the surface of the catalyst and retard the adsorption of CO_2 molecules, thus resulting in the decrease of CO yield.

The effect of the light wavelength on the photoactivity and selectivity was also investigated since semiconductor absorbs light radiation with a threshold wavelength which provides sufficient photon energy to overcome the bandgap. As shown in Figure 9, the CO yields are increased and CH_4 is produced as a minor product when the visible-light source is replaced by UV−vis light irradiation. The results show that the adjusting of the light source irradiation may not only tune the CO_2 photoreduction activity but also modulate the selectivity for the synthesized composites. The influence of the light intensity is also shown in Figure 9. Both CO, as a main product, and CH_4, as a minor product, are produced at the light intensity of 164 and 260 mW cm^{-2}, respectively. Nonetheless, the total yields of the later increased significantly in comparison with that of the former. The results suggest that the photocatalytic property is closely related to the intensity of irradiation light, consistent with that previously stated by Mao and co-workers.[51]

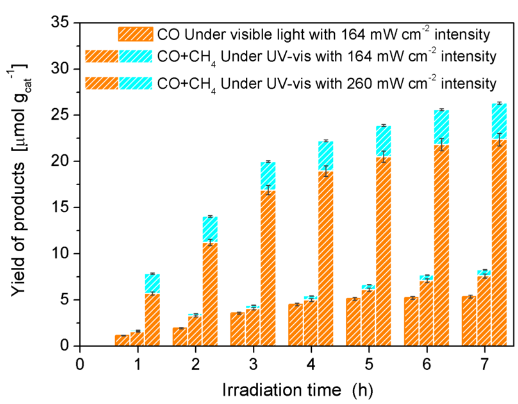

Figure 9. Total yields of the products over the 50Cu−Fe catalyst under different light source irradiation for different time.

It is worth noting that desirable catalysts for the reduction of CO_2 should selectively convert CO_2 to CO as opposed to CH_4,[54] because CO can be reacted with H_2O via the water−gas shift to generate H_2, and this CO/H_2 mixture can be further used to generate liquid fuels using Fischer−Tropsch methods.[55] In the present work, it is demonstrated that the photoreduction CO_2 can be selectively produced to CO, and that the selectivity can be controlled by modulating the light wavelength. The results obtained herein probably imply greater significance for the potential application of the synthesized photocatalysts.

Reproducibility and durability are two critical issues for the long-term use of catalysts in practical applications. In the durability tests, the photoreduction CO_2 of the representative 50Cu−Fe catalyst was recycled three times. The catalyst could maintain good activity after three photoreaction cycles, although the yield of CO slightly decreased with recycle (Figure S9, Supporting Information). To illustrate the stability of the catalyst, we applied XPS measurements to detect the change of the chemical composition (Figures S10 and S11, Supporting Information). The results show that a small amount of Cu^+ is oxidized to Cu^{2+}, which may be the reason for the slight degradation of photocatalytic activity.

3.6. Possible Photocatalytic Mechanism. On the basis of the experimental results and the band alignment of the 50Cu−Fe sample (Figure 6), the enhanced photocatalytic CO_2 activity can be deduced as follows. In our experiment, the Cu_2O phase is formed by reduction of the deposited Cu_2O precursor on the surface of α-Fe_2O_3. Because Fe_2O_3 is an n-type semiconductor and Cu_2O is p-type, the p−n junctions would be formed at the interfacial phase, and thus, an inner electrical field would be established at the interfaces in the direction from the n-type Fe_2O_3 to p-type Cu_2O. Under light irradiation, the VB electrons of both Fe_2O_3 and Cu_2O could be excited up and the separation process of the photoexcited electron−hole pairs can be schematically described in Figure 10. If the photoexcited

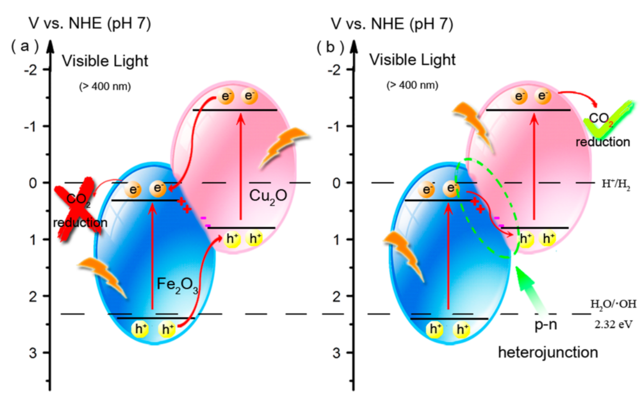

Figure 10. Schematic diagram of photoexicited electron−hole separation processes: (a) double-charge transfer mechanism and (b) Z-Scheme mechanism.

charge carriers transfer in the xCu−Fe heterojunction according to Figure 10a (i.e. adopting the common double-charge transfer mode), the accumulated electrons in the CB of Fe_2O_3 would not be able to reduce CO_2 to CO, because the CB potential of Fe_2O_3 (0.37 V vs. NHE) is more positive than the standard redox potential $E^{\theta}(CO_2/CO)$ (−0.53 V vs. NHE).

DOI: 10.1021/acsami.5b00822
ACS Appl. Mater. Interfaces 2015, 7, 8631−8639

Meanwhile, the capacity of h^+ in the VB of Cu_2O cannot oxidize water. Provided that the photoexcited electrons in the CB of Fe_2O_3 transfer directly to the VB of Cu_2O and recombine with the holes therein, it would result in accumulated abundant electrons in the CB of Cu_2O and holes in the VB of Fe_2O_3 to participate in the reduction and oxidation reactions, respectively. According to the promoted photocatalytic activity, the separation of photogenerated carriers is thought to be followed by the Z-scheme mechanism as, shown in Figure 10b. Consequently, the *x*Cu−Fe composites are a type of direct Z-scheme photocatalysts under our experimental conditions.

In light of the calculated band edge positions and the experimental results, the overall reduction mechanism of CO_2 to CO and CH_4 in the presence of water vapor can be inferred and expressed as

$$x\mathrm{Cu} - \mathrm{Fe} + h\nu \rightarrow h_{\mathrm{VB}}^{+} + e_{\mathrm{CB}}^{-} \quad (1)$$

$$\mathrm{H_2O} + h_{\mathrm{VB}}^{+} \rightarrow {}^{\bullet}\mathrm{OH} + \mathrm{H^+} \quad (2)$$

$${}^{\bullet}\mathrm{OH} + {}^{\bullet}\mathrm{OH} \rightarrow \mathrm{H_2O} + \frac{1}{2}\mathrm{O_2} \quad (3)$$

$$\mathrm{CO_2} + 2\mathrm{H^+} + 2e_{\mathrm{CB}}^{-} \rightarrow \mathrm{CO} + \mathrm{H_2O} \quad (4)$$

$$\mathrm{CO_2} + 8\mathrm{H^+} + 8e_{\mathrm{CB}}^{-} \rightarrow \mathrm{CH_4} + 2\mathrm{H_2O} \quad (5)$$

Because the electrons in the CB of Cu_2O in the composite have more negative potential (−1.32 eV), CO_2 can be reduced to yield CO ($E^\theta(CO_2/CO) = -0.53$ V) and CH_4 ($E^\theta(CO_2/CH_4) = -0.24$ V) thermodynamically. However, it is reported that the formation of products is decided kinetically by the number of electrons and protons taking part in the chemical reaction.[3] The formation of CO and CH_4 requires $2H^+/2e^-$ and $8H^+/8e^-$, respectively, according to eqs 4 and 5. Therefore, only those with shorter wavelength and stronger intensity could excite more electrons to the CB and result in not only more CO yield but also emerging CH_4. However, for the visible light irradiation, the number of the photogenerated electrons is insufficient to produce CH_4, thus resulting in the selectivity.

Besides the photogenerated electrons, the role of the concomitantly photogenerated holes cannot be ignored. At the surface the holes may react with adsorbed water to generate oxygen or hydroxide radicals (${}^\bullet$OH).[5] Considering that the valence band of the prepared catalysts (E^θ(VB) = 2.39 V) is located below the oxidation potential of water ($E^\theta(H_2O/{}^\bullet OH)$ = 2.32 V), the formation of hydroxyl radicals is a thermodynamically favored process. To gain more insight into the possible mechanism, hydroxyl radicals (${}^\bullet$OH) were detected by the PL method using TA as a probe molecule.[56] Figure 11 presents the PL spectral changes of the photocatalysts in the solution of TAOH (excitation at 315 nm) under visible-light illumination. An obvious increase of PL intensity at 425 nm is observed with prolonged irradiation time, indicating that the fluorescence comes from the chemical reactions between TA and ${}^\bullet$OH formed during photocatalytic process. Besides, the 50Cu−Fe sample shows a strong PL peak, while the pure materials appear no obvious peak at 425 nm (Figure S12, Supporting Information). Obviously, it is due to the high concentrations of holes in the composite that facilitate the generation of ${}^\bullet$OH species. These results show that the hydroxyl radicals are actually generated in the catalytic process and indeed participate in the photocatalytic reactions.

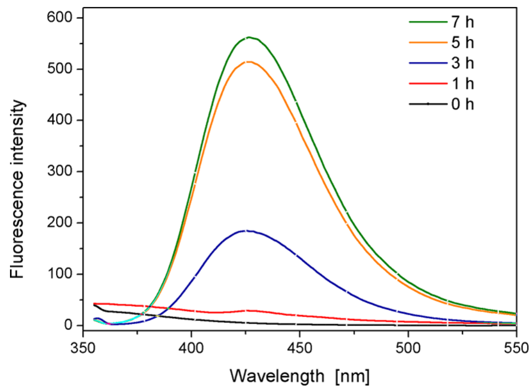

Figure 11. PL spectra for the 50Cu−Fe sample changing with the visible-light irradiation time with an excitation at 315 nm.

To further prove the suggested pathway, we measured the rate of O_2 generation under the condition of visible light irradiation with 164 mW cm^{-2} intensity, in the process of which only CO and O_2 were produced. It is proved that the rate of O_2 generation is about a half of that of CO (Figure S13, Supporting Information). The results supply another consolidated evidence for the above mechanism.

To provide convincing evidence for the separation of photogenerated electron−hole pairs, we recorded transient photocurrent responses of Fe_2O_3, Cu_2O, and 50Cu−Fe composite over several on−off irradiation cycles. Figure 12 shows a comparison of the *I*−*t* curves for these samples. As shown, the photocurrent response of the composite materials can reproducibly increase under each irradiation and quickly recover in the dark, consistent with the observations for other composites.[57,58] Moreover, the transient photocurrent of the composite is about 4 and 2 times higher than that of pure Fe_2O_3 and Cu_2O, respectively. The increased photocurrent responses of the composite suggest the higher separation efficiency of electron−hole pairs and a lower recombination rate in such heterostructure under visible-light irradiation.[25] The results can be explained by the Z-scheme transfer of electrons across the junctions from Fe_2O_3 to Cu_2O, which reduces the recombination of electron−hole pairs as discussed before. Hence, enhanced photocatalytic activity can be anticipated for the *x*Cu−Fe heterostructures. Besides transient photocurrent, the results of electrochemical impedance spectroscopy (EIS) and photoluminescence (PL) emission spectra

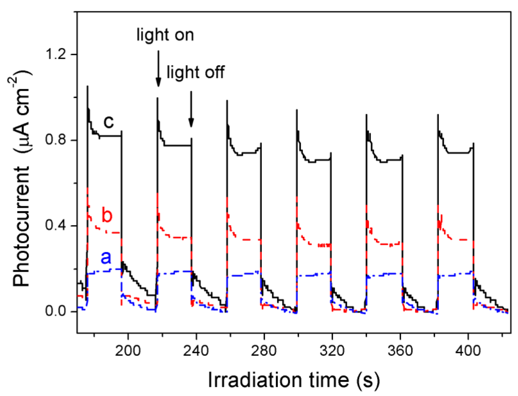

Figure 12. Transient photocurrent responses for (a) Fe_2O_3, (b) Cu_2O, and (c) 50Cu−Fe.

DOI: 10.1021/acsami.5b00822
ACS Appl. Mater. Interfaces 2015, 7, 8631−8639

also provide strong supports for the separation of electron−hole pairs (see Figure S14 and Figure S15, Supporting Information).

Based on the above analyses, it is clear that the charge transfer for the composite photocatalysts agrees well with the process shown in Figure 10b and the *x*Cu−Fe composites are indeed typical Z-scheme photocatalysts.

4. CONCLUSIONS

Z-scheme *x*Cu−Fe photocatalysts are achieved successfully by facile hydrothermal-deposition followed by reduction process. The *x*Cu−Fe composites exhibit good photocatalytic activity of CO_2 reduction under visible light (>400 nm). The optimal content of Cu_2O in the composites is found to be 50 mol %, and the CO yield is 5.0 μmol g_{cat}^{-1} after irradiation for 3 h. The yields of the products change with the H_2O/CO_2 molar ratio, and the type of product varies with the light wavelength. The enhanced photoactivity is ascribed to the efficient separation of the photoinduced electron−hole pairs derived from the constructed composite structure. A Z-scheme transfer mechanism is proposed and further confirmed by the detection of hydroxyl radicals. The knowledge gained herein may provide some insights into the design of Z-scheme heterostructures with engineered band structure and has important implications in solar VLD catalysis.

■ ASSOCIATED CONTENT

Supporting Information

Additional characterization and photoelectrochemical data. This material is available free of charge via the Internet at http://pubs.acs.org.

■ AUTHOR INFORMATION

Corresponding Authors

*E-mail: yaohongchang@zzu.edu.cn.

*E-mail: lizhongjun@zzu.edu.cn.

Notes

The authors declare no competing financial interest.

■ ACKNOWLEDGMENTS

This work was supported by the financial supports of the National Natural Science Found of China (Nos. 21471133 and J1210060), Foundation of He'nan Educational Committee, China (Nos. 14A150001 and 13A150455) and Key Science and Technology Program of Zhengzhou, China (No: 141PQYJS562).

■ REFERENCES

(1) D'Alessandro, D. M.; Smit, B.; Long, J. R. Carbon Dioxide Capture: Prospects for New Materials. *Angew. Chem., Int. Ed.* **2010**, *49*, 6058−6082.

(2) Lal, R. Sequestration of Atmospheric CO_2 in Global Carbon Pools. *Energy Environ. Sci.* **2008**, *1*, 86−100.

(3) Tu, W.; Zhou, Y.; Zou, Z. Photocatalytic Conversion of CO_2 into Renewable Hydrocarbon Fuels: State-of-the-Art Accomplishment, Challenges, and Prospects. *Adv. Mater.* **2014**, *26*, 4607−4626.

(4) Roy, S. C.; Varghese, O. K.; Paulose, M.; Grimes, C. Toward Solar Fuels: Photocatalytic Conversion of Carbon Dioxide to Hydrocarbons. *ACS Nano* **2010**, *4*, 1259−1278.

(5) Habisreutinger, S. N.; Schmidt-Mende, L.; Stolarczyk, J. K. Photocatalytic CO_2 Reduction by TiO_2 and Related Titanium containing Solids. *Angew. Chem., Int. Ed.* **2013**, *52*, 7372−7408.

(6) Inoue, T.; Fujimshima, A.; Konishi; Honda, K. Photoelectrocatalytic Reduction of Carbon Dioxide in Aqueous Suspensions of Semiconductor Powers. *Nature* **1979**, *277*, 637−638.

(7) Dhakshinamoorthy, A.; Navalon, S.; Corma, A.; Garcia, H. Photocatalytic CO_2 Reduction by TiO_2 and Related Titanium Containing Solids. *Energy Environ. Sci.* **2012**, *5*, 9217−9233.

(8) Tahir, M.; Amin, N. S. Advances in Visble Light Responsive Titanium Oxide-based Photocatalyts for CO_2 Conversion to Hydrocarbon Fuels. *Energy Convers. Manage* **2013**, *76*, 194−214.

(9) Liu, Y.; Huang, B.; Dai, Y.; Zhang, X.; Qin, X.; Jiang, M.; Whangbo, M.-H. Selective Ethanol Formation from Photocatalytic Reduction of Carbon Dioxide in Water with $BiVO_4$ Photocatalyst. *Catal. Commun.* **2009**, *11*, 210−213.

(10) Cheng, H.; Huang, B.; Liu, Y.; Wang, Z.; Qin, X.; Zhang, X.; Dai, Y. An Anion Exchange Approach to Bi_2WO_6 Hollow Microspheres with Efficient Visble Light Photocatalytic Reduction of CO_2 to Methanol. *Chem. Commun.* **2012**, *48*, 9729−9731.

(11) Handoko, A. D.; Tang, J. Controllable Proton and CO_2 Photoreduction over Cu_2O with Various Morphologies. *Int. J. Hydrogen Energy* **2013**, *38*, 13017−13022.

(12) Wang, H.; Zhang, L.; Chen, Z.; Hu, J.; Li, S.; Wang, Z.; Liu, J.; Wang, X. Semiconductor Heterojunction Photocatalysts: Design, Construction, and Photocatalytic Performances. *Chem. Soc. Rev.* **2014**, *43*, 5234−5244.

(13) Qu, Y.; Duan, X. Progress, Challenge, and Perspective of Heterogeneous Photocatalysts. *Chem. Soc. Rev.* **2013**, *42*, 2568−2580.

(14) Wang, Y.; Wang, Q.; Zhan, X.; Wang, F.; Safdar, M.; He, J. Visible Light Driven Type II Heterostructures and Their Enhanced Photocatalysis Properties: A Review. *Nanoscale* **2013**, *5*, 8326−8339.

(15) Zhou, P.; Yu, J.; Jaroniec, M. All-Solid-State Z-Scheme Photocatalytic Systems. *Adv. Mater.* **2014**, *26*, 4920−4935.

(16) Wang, X.; Yin, L.; Liu, G. Light Irradiation-Assisted Synthesis of ZnO−CdS/Reduced Graphene Oxide Heterostructured Sheets for Efficient Photocatalytic H_2 Evolution. *Chem. Commun.* **2014**, *50*, 3460−3463.

(17) Jia, Q.; Iwase, A.; Kudo, A. $BiVO_4$−Ru/$SrTiO_3$:Rh Composite Z-Scheme Photocatalyst for Solar Water Splitting. *Chem. Sci.* **2014**, *5*, 1513−1519.

(18) Min, Y. L.; He, G. Q.; Xu, Q. J.; Chen, Y. C. Self-Assembled Encapsulation of Graphene Oxide/Ag@AgCl as a Z-Scheme Photocatalytic System for Pollutant Removal. *J. Mater. Chem. A* **2014**, *2*, 1294−1301.

(19) Sato, S.; Arai, T.; Morikawa, T.; Uemura, K.; Suzuki, T. M.; Tanaka, H.; Kajino, T. Selective CO_2 Conversion to Formate Conjugated with H_2O Oxidation Utilizing Semiconductor/ Complex Hybrid photocatalysts. *J. Am. Chem. Soc.* **2011**, *133*, 15240−15243.

(20) Sekizawa, K.; Maeda, K.; Domen, K.; Koike, K.; Ishitani, O. Artificial Z-Scheme Constructed with a Supramolecular Metal Complex and Semiconductor for the Photocatalytic Reduction of CO_2. *J. Am. Chem. Soc.* **2013**, *135*, 4596−4599.

(21) Zhou, X.; Yang, H.; Wang, C.; Mao, X.; Wang, Y.; Yang, Y.; Liu, G. Visible Light Induced Photocatalytic Degradation of Rhodamine B on One-Dimensional Iron Oxide Particles. *J. Phys. Chem. C* **2010**, *114*, 17051−17061.

(22) Zhong, D. K.; Sun, J.; Inumaru, H.; Gamelin, D. R. Solar Water Oxidation by Composite Catalyst/α-Fe_2O_3 Photoanodes. *J. Am. Chem. Soc.* **2009**, *131*, 6086−6087.

(23) Zhang, Q.; Gao, T.; Andino, J. M.; Li, Y. Copper and Iodine Co-modified TiO_2 Nanoparticles for Improved Activity of CO_2 Photoreduction with Water Vapor. *Appl. Catal., B* **2012**, *123*−*124*, 257−264.

(24) Li, Y.; Wang, W.-N.; Zhan, Z.; Woo, M.-H.; Wu, C.-Y.; Biswas, P. Photocatalytic Reduction of CO_2 with H_2O on Mesoporous Silica Supported Cu/TiO_2 Catalysts. *Appl. Catal. B: Environ.* **2010**, *100*, 386−392.

(25) Zhai, Q.; Xie, S.; Fan, W.; Zhang, Q.; Wang, Y.; Deng, W.; Wang, Y. Photocatalytic Conversion of Carbon Dioxide with Water into Methane: Platinum and Copper(I) Oxide Co-catalysts with a Core−Shell Structure. *Angew. Chem., Int. Ed.* **2013**, *52*, 5776−5779.

DOI: 10.1021/acsami.5b00822
ACS Appl. Mater. Interfaces 2015, 7, 8631−8639

(26) Townsend, T. K.; Sabio, E. M.; Browning, N. D.; Osterloh, F. E. Photocatalytic Water Oxidation with Suspended α-Fe_2O_3 Particles-Effects of Nanoscaling. *Energy Environ. Sci.* **2011**, *4*, 4270−4275.

(27) Paracchino1, A.; Laporte, V.; Sivula, K.; Grätzel, M.; Thimsen, E. Highly Active Oxide Photocathode for Photoelectrochemical Water Reduction. *Nat. Mater.* **2011**, *10*, 456−461.

(28) Mirtchev, P.; Liao, K.; Jaluague, E.; Qiao, Q.; Tian, Y.; Varela, M.; Burch, K. S.; Pennycook, S. J.; Perovic, D. D.; Ozin, G. Fe_2O_3/Cu_2O Heterostructured Nanocrystals. *J. Mater. Chem. A* **2014**, *2*, 8525−8533.

(29) Linsebigler, A. L.; Lu, G.; Yates, J. T., Jr. Photocatalysis on TiO_2 Surfaces: Principles, Mechanisms, and Selected Results. *Chem. Rev.* **1995**, *95*, 735−758.

(30) Hagfeldtt, A.; Gratzel, M. Light-Induced Redox Reactions in Nanocrystalline Systems. *Chem. Rev.* **1995**, *95*, 49−68.

(31) Kirchartz, T.; Matteis, J.; Rau, U. Detailed Balance Theory of Excitonic and Bulk Heterojunction Solar Cells. *Phys. Rev. B* **2008**, *78*, 235320.

(32) Chen, J.; Shen, S.; Guo, P.; Wang, M.; Wu, P.; Wang, X.; Guo, L. In Situ Reduction Synthesis of Nano-sized Cu_2O Particles Modifying g-C_3N_4 for Enhanced Photocatalytic Hydrogen Production. *Appl. Catal. B: Environ.* **2014**, *152*−*153*, 335−341.

(33) Liu, J.; Gao, Z.; Han, H.; Wu, D.; Xu, F.; Wang, H.; Jiang, K. Mesoporous Cu_2O Submicro-Spheres, Facile Synthesis and the Selective Adsorption Properties. *Chem. Eng. J.* **2012**, *185*−*186*, 151−159.

(34) Kwok, R. W. M. Department of Chemistry, The Chinese University of Hong Kong, Shatin, Hong Kong. Available from: http://www.uksaf.org/software.html.

(35) Chen, Z.; Fang, L.; Dong, W.; Zheng, F.; Shen, M.; Wang, J. Inverse Opal Structured Ag/TiO_2 Plasmonic Photocatalyst Prepared by Pulsed Current Deposition and its Enhanced Visible Light Photocatalytic Activity. *J. Mater. Chem. A* **2014**, *2*, 824−832.

(36) Charbouillot, T.; Brigante, M.; Mailhot, G.; Maddigapu, P. R.; Minero, C.; Vione, D. Performance and Selectivity of the Terephthalic Acid Probe for $^{\bullet}$OH as a Function of Temperature, pH, and Composition of Atmospherically Relevant Aqueous Media. *J. Photochem. Photobio. A* **2011**, *222*, 70−76.

(37) Kwon, K.-W.; Shim, M. γ-Fe_2O_3/II-VI Sulfide Nanocrystal Heterojunctions. *J. Am. Chem. Soc.* **2005**, *127*, 10269−10275.

(38) Li, P.; Jang, H.; Xu, J.; Wu, C.; Peng, H.; Lu, J.; Lu, F. High-efficiency Synergistic Conversion of CO_2 to Methanol using Fe_2O_3 Nanotubes Modified with Double-Layer Cu_2O Spheres. *Nanoscale* **2014**, *6*, 11380−11386.

(39) Yamashita, T.; Hayes, P. Analysis of XPS Spectra of Fe^{2+} and Fe^{3+} Ions in Oxide Materials. *Appl. Surf. Sci.* **2008**, *254*, 2441−2449.

(40) Balamurugan, B.; Mehta, B. R.; Shivaprasad, S. M. Surface-modified CuO Layer in Size-Stabilized Single-Phase Cu_2O Nanoparticles. *Appl. Phys. Lett.* **2001**, *79*, 3176−3179.

(41) Yin, M.; Wu, C.-K.; Lou, Y.; Burda, C.; Koberstein, J. T.; Zhu, Y.; O'Brien, S. Copper Oxide Nanocrystals. *J. Am. Chem. Soc.* **2005**, *127*, 9506−9511.

(42) Ikeue, K.; Yamashita, H.; Anpo, M. Photocatalytic Reduction of CO_2 with H_2O on Ti-β-Eolite Photocatalysts: Effect of the Hydrophobic and Hydrophilic Properties. *J. Phys. Chem. B* **2001**, *105*, 8350−8355.

(43) Gao, B.; Liu, L.; Liu, J.; Yang, F. Photocatalytic Degradation of 2,4,6-Tribromophenol on Fe_2O_3 or FeOOH Doped $ZnIn_2S_4$ Heterostructure: Insight into Degradation Mechanism. *Appl. Catal. B: Environ.* **2014**, *147*, 929−939.

(44) Jongh, P. E.; Vanmaekelbergh, D.; Kelly, J. J. Cu_2O: Electrodeposition and Characterization. *Chem. Mater.* **1999**, *11*, 3512−3517.

(45) Pradhan, G. K.; Parida, K. M. Fabrication, Growth Mechanism, and Characterization of α-Fe_2O_3 Nanorods. *ACS Appl. Mater. Interfaces* **2011**, *3*, 317−323.

(46) Xiao, G.; Wang, X.; Li, D.; Fu, X. $InVO_4$-Sensitized TiO_2 Photocatalysts for Efficient Air Purification with Visible Light. *J. Photochem. Photobiol., A* **2008**, *193*, 213−221.

(47) Jiang, J.; Zhang, X.; Sun, P.; Zhang, L. ZnO/BiOI Heterostructures: Photoinduced Charge-Transfer Property and Enhanced Visible-Light Photocatalytic Activity. *J. Phys. Chem. C* **2011**, *115*, 20555−20564.

(48) Kraut, E. A.; Grant, R. W.; Waldrop, J. R.; Eowalczyk, S. P. Precise Determination of the Valence-Band Edge in X-ray Photoemission Spectra: Application to Measurement of Semiconductor Interface Potentials. *Phys. Rev. Lett.* **1980**, *44*, 1620−1623.

(49) Kramm, B.; Laufer, A.; Reppin, D.; Kronenberger, A.; Hering, P.; Polity, A.; Meyer, B. K. The Band Alignment of Cu_2O/ZnO and Cu_2O/GaN Heterostructures. *Appl. Phys. Lett.* **2012**, *100*, 094102.

(50) Sharma, B. L.; Purohit, R. K. *Semiconductor Heterojunctions*. Pergamon Press: New York,1974.

(51) Mao, J.; Li, K.; Peng, T. Recent Advances in the Photocatalytic CO_2 Reduction over Semiconductors. *Catal. Sci. Technol.* **2013**, *3*, 2481−2498.

(52) Fox, M. A.; Dulay, M. T. Heterogeneous Photocatalysis. *Chem. Rev.* **1993**, *93*, 341−357.

(53) Zhang, Q.-H.; Han, W.-D.; Hong, Y.-J.; Yu, J.-G. Photocatalytic Reduction of CO_2 with H_2O on Pt-Loaded TiO_2 Catalyst. *Catal. Today* **2009**, *148*, 335−340.

(54) Jiang, Z.; Xiao, T.; Kuznetsov, V. L.; Edwards, P. P. Turning Carbon Dioxide into Fuel. *Philos. Trans. R. Soc., A* **2010**, *368*, 3343−3364.

(55) Takeshita, T.; Yamaji, K. Important Roles of Fischer−Tropsch Synfuels in the Global Energy Future. *Energy Policy* **2008**, *36*, 2773−2784.

(56) Yu, J.; Wang, S.; Low, J.; Xiao, W. Enhanced Photocatalytic Performance of Direct Z-Scheme g-C_3N_4-TiO_2 Photocatalysts for the Decomposition of Formaldehyde in Air. *Phys. Chem. Chem. Phys.* **2013**, *15*, 16883−16890.

(57) Cao, S.-W.; Liu, X.-F.; Yuan, Y.-P.; Zhang, Z.-Y.; Liao, Y.-S.; Fang, J.; Loo, S. C. J.; Sum, T. C.; Xu, C. Solar-to-Fuels Conversion over In_2O_3/g-C_3N_4 Hybrid Photocatalysts. *Appl. Catal., B* **2014**, *147*, 940−946.

(58) Li, P.; Zhao, X.; Jia, C.-J.; Sun, H.; Sun, L.; Cheng, X.; Liu, L.; Fan, W. $ZnWO_4$/BiOI Heterostructures with Highly Efficient Visible Light Photocatalytic Activity: The Case of Interface Lattice and Energy Level Match. *J. Mater. Chem. A* **2013**, *1*, 3421−3429.

DOI: 10.1021/acsami.5b00822
ACS Appl. Mater. Interfaces 2015, 7, 8631−8639